Journal of Hazardous Materials 180 (2010) 409–418

Contents lists available at ScienceDirect

Journal of Hazardous Materials

journal homepage: www.elsevier.com/locate/jhazmat

Carbon deposition and phase transformations in red mud on exposure to methane

S. Sushil[a], A.M. Alabdulrahman[b], M. Balakrishnan[a], V.S. Batra[a,*], R.A. Blackley[c], J. Clapp[d], J.S.J. Hargreaves[d], A. Monaghan[d], I.D. Pulford[d], J.L. Rico[e], W. Zhou[c]

[a] Centre for Energy and Environment, TERI University, Darbari Seth Block, Habitat Place, Lodhi Road, New Delhi 110003, India
[b] King Abdulaziz City for Science and Technology (KACST), Petroleum and Petrochemical Research Institute (PAPRI), PO Box 6086, Riyadh 11442, Saudi Arabia
[c] School of Chemistry, University of St. Andrews, North Haugh, St. Andrews KY16 9ST, UK
[d] WestCHEM, Department of Chemistry, Joseph Black Building, University of Glasgow, Glasgow G12 8QQ, UK
[e] Laboratorio de Catálisis, Facultad de Ingeniería Química, Universidad Michoacana de San Nicolás de Hidalgo, Edificio E, CU, Morelia, Mich. C.P. 58060, Mexico

ARTICLE INFO

Article history:
Received 6 March 2010
Received in revised form 2 April 2010
Accepted 12 April 2010
Available online 18 April 2010

Keywords:
Red mud
Methane
Decomposition
Carbon nanostructures

ABSTRACT

A characterization study detailing the phase transformations and microstructural nature of the carbon deposited during methane decomposition over red mud has been undertaken. *In situ* XRD was carried out to study the phase transformation sequences of red mud during the reaction. Scanning electron microscopy, high resolution transmission electron microscopy, thermogravimetric analysis, BET surface area determination and CHN analysis were carried out to investigate the properties of the post-reaction samples. Exposure to methane with increasing temperature caused a stepwise reduction of iron oxides in red mud and promoted methane cracking leading to carbon deposition. The presence of carbon nanostructures was confirmed by HRTEM observations. The carbon formed was graphitic in nature and the spent red mud, rich in Fe and Fe_3C formed as a result of the reduction of the iron oxide, was magnetic in nature. The surface area of the material was enhanced upon reaction. In addition, reactivity comparisons between goethite and red mud were carried out to study the formation of carbon oxides during reaction.

1. Introduction

Transition metals such as nickel, iron and cobalt are known to be active for the decomposition of hydrocarbons [1]. Such reactions are of importance since the final products include hydrogen which is free from the presence of CO_x and which therefore may find application in PEM (Proton Exchange Membrane) fuel cells. In addition to this, these reactions are considered more simple as compared to the conventional methods of hydrogen production [2]. During the decomposition of hydrocarbons, carbon deposition also takes place [3,4]. Over the years, a number of studies of the structural and morphological characteristics of such carbon have been undertaken with the primary aim of determining the mechanism of its formation [5–8]. The carbon filaments which are often reported to be formed have a number of potential applications such as adsorbents, catalyst supports and reinforcement materials [9–11].

Red mud, a by-product of the aluminium industry, consists of a mixture of metal oxides. The major component is iron oxide while other components include oxides of Al, Si, Ti, Ca, and Na [12–14]. Since iron derived from the reduction of iron oxides is known to be an active catalyst [4], red mud may be considered as potentially active for hydrocarbon decomposition.

Carbon formation via methane decomposition is based on the following reaction:

$$CH_4 \rightarrow 2H_2 + C$$

Graphitic carbons are generally formed at reaction temperatures higher than 500 °C, while at low reaction temperatures, both carbidic and graphitic carbons may be observed [2]. Narkiewics et al. [15] investigated the formation of carbon on metal surfaces via hydrocarbon decomposition leading to the formation of atomic carbon. The atomic carbon may give rise to amorphous carbon and graphitic carbon by undergoing polymerization or it may lead to the formation of carbide by dissolution into the metal lattice. Carbon fibres are formed by segregation of the carbon dissolved in metal. The properties of the carbon produced may vary depending on the composition of the catalyst, gas composition and other reaction variables such as temperature. It has been reported that chaotically interlaced filaments are generally formed in the case of methane decomposition [16].

* Corresponding author. Fax: +91 11 24682144.
E-mail address: vidyasb@teri.res.in (V.S. Batra).

0304-3894/$ – see front matter © 2010 Elsevier B.V. All rights reserved.
doi:10.1016/j.jhazmat.2010.04.046

We have previously reported the production of hydrogen from methane in the presence of a variety of red mud samples obtained from India [17]. The highest methane conversion obtained was 19.8% with a corresponding methane conversion rate of 18.0×10^{-6} mol CH_4 g^{-1} s^{-1} [17]. The spent red mud was magnetic in nature due to the presence of Fe and Fe_3C [17]. In the current study we report the transformations occurring in red mud as well as the formation of CO_x during the reaction. Microstructural analysis of the resultant carbon has also been undertaken.

2. Experimental

Red mud from three different sources (RM 4, RM 6 and RM 7) was tested. These are the same samples which had been examined previously and their composition and phase analysis has been reported elsewhere [17]. Goethite is present in fresh red mud used for the reaction; however it is mixed with many other phases. Therefore, for the sake of comparison synthetic goethite prepared in the lab was also tested under similar conditions.

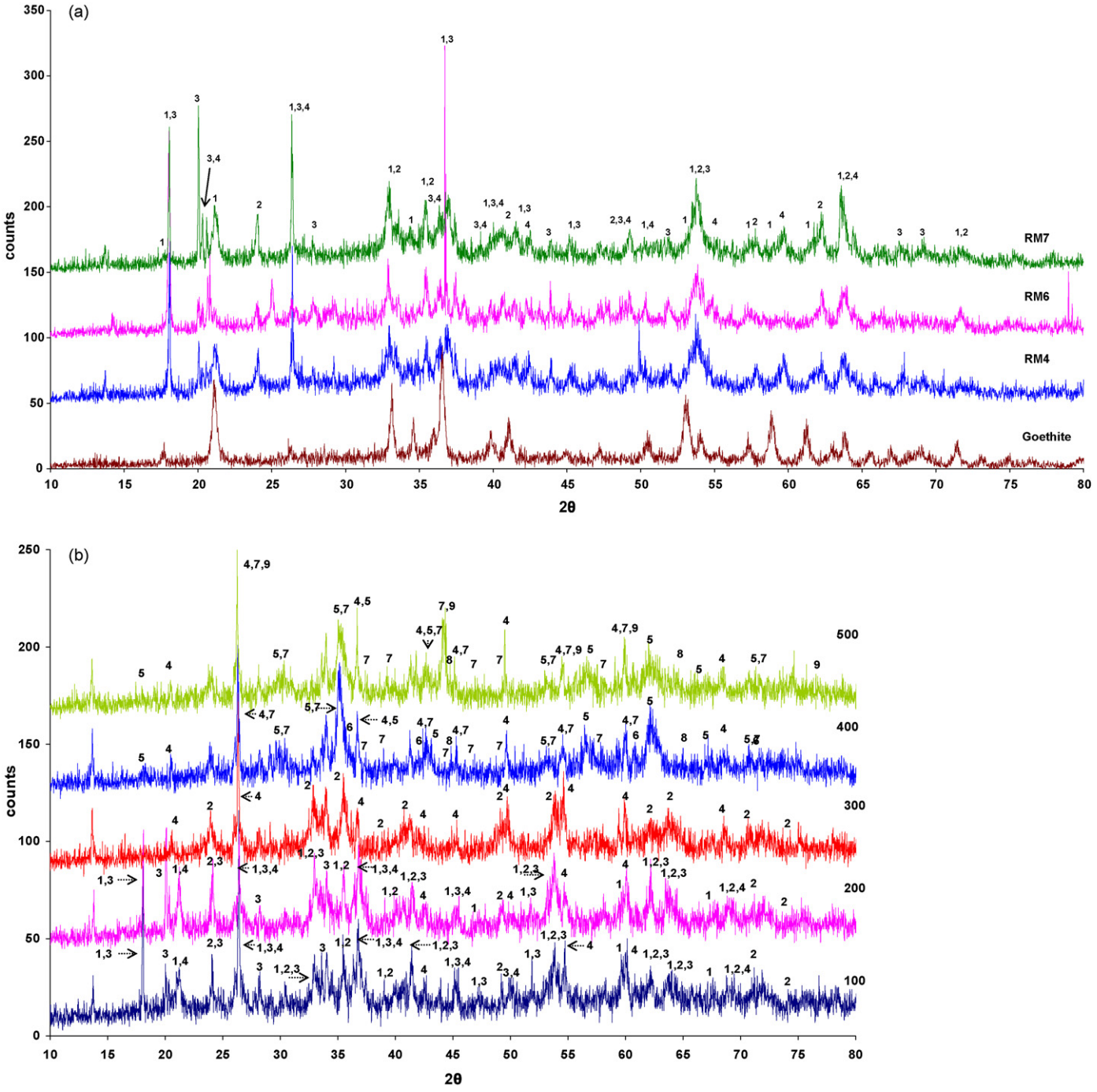

Fig. 1. (a) XRD patterns for as-received red mud (RM 4, RM 6 and RM 7) and synthetic goethite; 1: goethite FeO(OH); 2: haematite Fe_2O_3; 3: gibbsite $Al_2O_3{\cdot}3H_2O$; 4: quartz SiO_2. (b) XRD patterns obtained in the presence of pure methane for RM 4; 1: goethite FeO(OH); 2: haematite Fe_2O_3; 3: gibbsite $Al_2O_3{\cdot}3H_2O$; 4: quartz SiO_2; 5: magnetite Fe_3O_4; 6: wustite FeO; 7: cementite Fe_3C; 8: iron Fe; 9: cliftonite C. (c) XRD patterns obtained in the presence of pure methane for RM 6; 1: haematite Fe_2O_3; 2: magnetite Fe_3O_4; 3: quartz SiO_2; 4: gibbsite $Al_2O_3{\cdot}3H_2O$, 5: anatase TiO_2; 6: pseudorutile $Fe_2Ti_3O_9$; 7: wustite FeO; 8: iron Fe; 9: cementite Fe_3C; 10: aluminium oxide Al_2O_3; 11: cliftonite C. (d) Post *in situ* XRD pattern obtained in the presence of pure methane for RM 4; 1: iron Fe; 2: cliftonite C; 3: cementite Fe_3C.

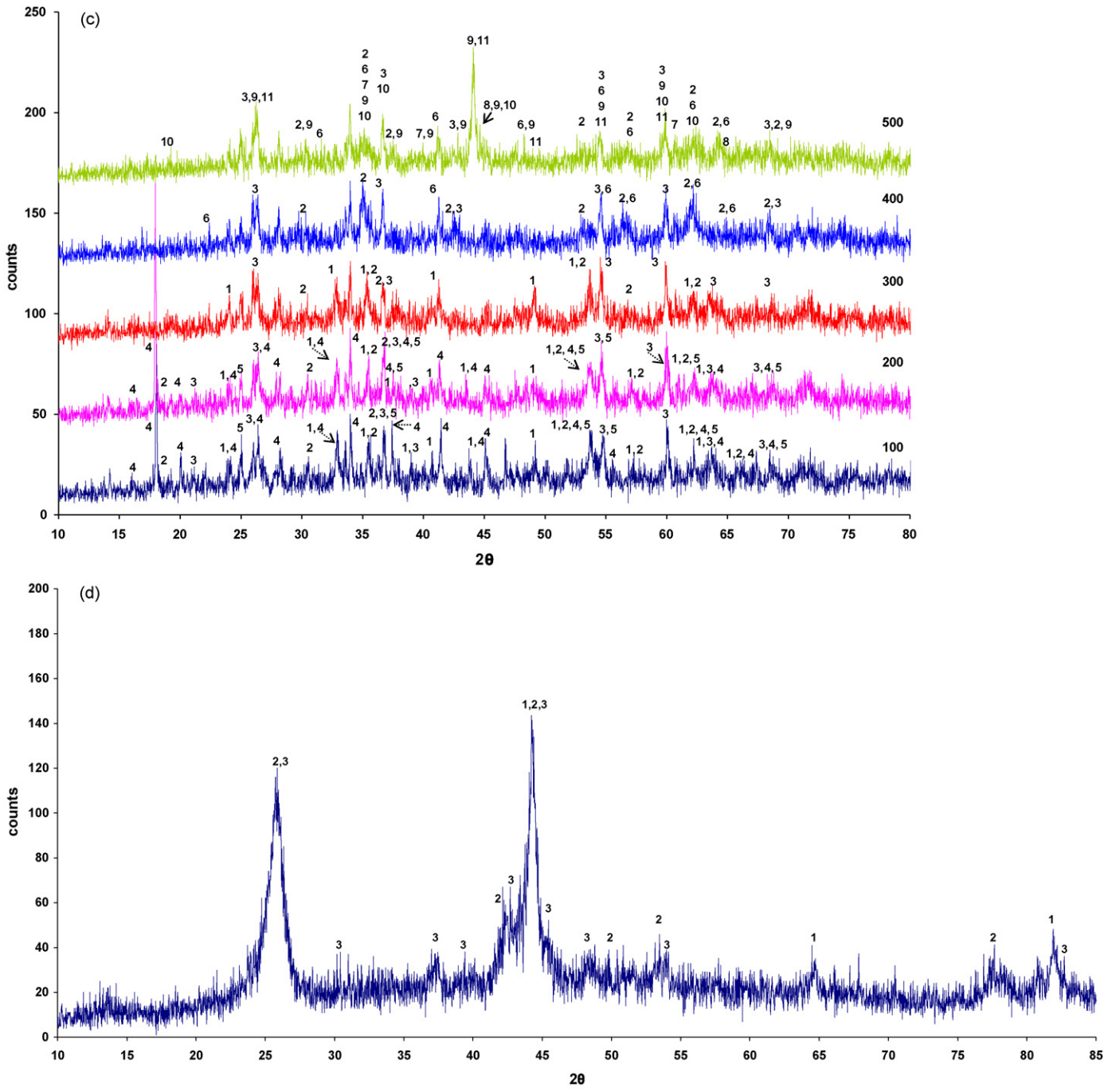

Fig. 1. (*Continued*).

The preparation of goethite was based upon a method reported by Cornell and Schwertmann [18]. 100 ml of 1 M $Fe(NO_3)_3$ solution (freshly prepared by the dissolution of $Fe(NO_3)_3{\cdot}9H_2O$ (Aldrich) in distilled water) was poured into a polypropylene bottle followed by the rapid addition of 180 ml of 5 M KOH (Aldrich) solution with stirring. The resultant suspension was then diluted to 2 l with distilled water. The bottle was sealed and the mixture aged at 70 °C for 60 h in an oven. Upon removal from the oven, the resultant goethite was separated by centrifugation, prior to being washed and then dried overnight at 80 °C.

The as-received red mud samples were subjected to *in situ* XRD using a Siemens D5000 diffractometer equipped with an Anton-Paar XRK reaction cell. The samples were heated from room temperature at a rate of 10 °C/min under a 20 ml/min flow of CH_4 (BOC, 99.5%) and scans were taken at 100 °C intervals between 100 and 700 °C. Cu K_α radiation was used and the 2θ range investigated was 10–80°, with a step size of 0.02° and a counting rate of 2 s per step.

The reactor and procedures employed for catalytic activity determination have been reported elsewhere [17]. In addition, CO_x quantification was undertaken by FTIR analysis of aliquots of the effluent reactor stream which were sampled by passage through a gas-phase FTIR cell. FTIR analysis was undertaken using a Jasco 4100 FTIR Spectrometer operating in the 400–4000 cm^{-1} spectral range acquiring 64 scans for each spectrum at a resolution of 4 cm^{-1} following background subtraction. A limitation of this method is that it becomes insensitive to CO_2 levels below those used for the background subtraction.

The samples obtained after exposure to methane in the *in situ* XRD and reactor experiments were further characterized by scanning electron microscopy (SEM), high resolution transmission electron microscopy (HRTEM), CHN analysis, thermogravimetric analysis (TGA) in a 2% O_2–Ar atmosphere and BET surface area analysis. SEM was undertaken in an XL30 ESEM Phillips microscope operating at 20 kV. HRTEM was performed using two instruments. The first was a Technai G20-stwin (200 kV) with super twin lenses in which the point resolution was 1.44 Å and line resolution of 2.32 Å. HRTEM was also performed on a JEM 2011 fitted with a LaB_6 filament and a resolution of 1.8 Å. CHN was determined by combustion using an Exeter Analytical CE-440 elemental analyzer. TGA was performed using a TA Instruments SDT Q600 instrument with measurements being undertaken in the temperature range from ambient to 800 °C at a heating rate of 10 °C/min. BET surface areas were measured with a SMART Instrument model 92/93 using N_2 physisorption at liquid nitrogen temperature (−196 °C) following appropriate degassing of samples.

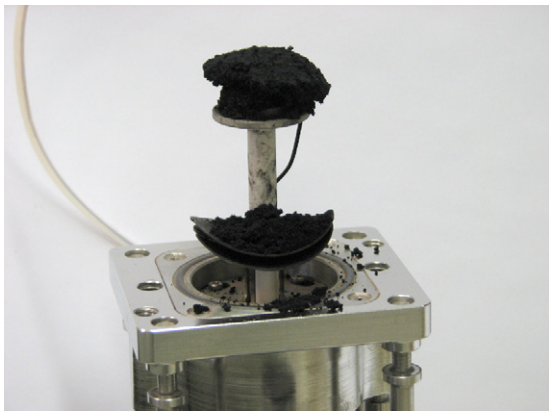

Fig. 2. Photograph of XRD sample holder showing a huge increase in volume of RM 4 after heating in methane atmosphere—the sample had originally been level with the top of the white ceramic holder.

3. Results

3.1. In situ XRD studies

The composition of the as-received red mud samples has been reported previously [17]. The main components are Fe_2O_3 (36–43%), Al_2O_3 (10–24%), SiO_2 (12–17%) and TiO_2 (0.7–19%). In addition to these, other minor components present include Na_2O, CaO, MgO, etc. XRD patterns for the as-received red mud samples (RM 4, RM 6 and RM 7) [17] and synthetic goethite is shown in Fig. 1a. The main phase identified in all red mud samples was haematite (Fe_2O_3). Other phases present were goethite, gibbsite and quartz. An additional phase identified in RM 6 was anatase. The patterns of the red mud samples recorded *in situ* under a CH_4 atmosphere at 100 °C were found to be similar to those for the as-received red mud samples. The powder diffraction pattern of the synthetic goethite precursor confirms that α-FeOOH is the major phase present (Fig. 1a). However, the background indicates the presence of some amorphous material. The goethite reflections are narrow which indicates the coherent diffraction domains to be large, suggesting large crystallites which are well ordered.

Fig. 1b shows the major phases present at different temperatures for RM 4, which was the most active sample for methane decomposition during the reactor run. Transformation of the iron and aluminium hydroxide based phases is seen by the loss of reflections corresponding to goethite (α-FeOOH) and gibbsite ($Al(OH)_3$) respectively due to the increase in the temperature. Up to 200 °C the main iron containing phases present are goethite and haematite. As a result of the dehydration due to the high temperature the goethite peaks are no longer apparent at 300 °C and only haematite peaks can be seen. Throughout the experiment, iron phases with various stages of reduction can be observed. At 400 °C, reduction of haematite to yield magnetite is observed. Low intensity wustite peaks are also seen at 400 °C. Both iron and iron carbide start to appear at 400 °C, however the peaks are not very intense at this stage. At 500 °C graphite is also evident along with magnetite, iron carbide and iron.

The phase transformation sequences for RM 6 and RM 7 were similar to those evident in RM 4. However in case of RM 6 (Fig. 1c) the formation of intermediate compounds of iron and titanium could also be observed. The reflections observed in RM 6 at 100, 200 and 300 °C could be indexed to haematite and magnetite. At 400 °C the haematite peaks are not very obvious while the magnetite peaks can still be seen. In addition, pseudorutile ($Fe_3Ti_2O_9$) also appears to be present. Anatase was identified in the RM 6 samples at lower temperatures. At 500 °C additional reflections of magnetite, wustite, iron carbide, and iron are also seen.

Due to a large increase in volume of the sample as a result of coke formation, the scans at temperatures higher than 500 °C did not show clear peaks. It is important to appreciate that all the *in situ* XRD samples have been exposed to methane at 700 °C. Subsequent analysis demonstrated the presence of graphite, iron and iron carbide in the samples. Fig. 1d shows the post *in situ* XRD pattern for RM 4. Here the presence of iron, carbon and iron carbide is seen. Fig. 2 is a photograph of the sample holder after the *in situ* reaction in which the large expansion of sample volume can be seen. Similar to the post-reaction samples observed in our previous study [17], the post *in situ* XRD sample was magnetic.

3.2. Scanning electron microscopy

SEM images of the samples were taken after the *in situ* XRD reactions (Fig. 3a–c).

Carbon deposits as filamentous structures of different diameter and lengths were seen to have grown on the samples. The filaments seen in case of RM 4 and RM 7 are convoluted and intertwined. Such structures have been reported by others to grow on iron catalysts [19]. RM 6 shows negligible growth of any carbon structures.

3.3. CHN analysis

Table 1 shows the results of the CHN analysis of red mud samples before and after exposure to pure methane during *in situ* XRD.

From the results it is clear that there is significant deposition of carbon in RM 4 and RM 7, with a higher amount of carbon deposition in the latter. Although the quantity of carbon deposited over RM 6 is much less than in the case of the other two samples, it is still significant.

Table 1
CHN analysis of red mud samples before and after exposure to *in situ* XRD in methane.

Sample	Mean value, wt%		
	C	H	N
RM 4	0.7	1.6	–
RM 4 post *in situ* XRD	63.7	–	–
RM 6	1.7	1.2	–
RM 6 post *in situ* XRD	27.8	–	–
RM 7	1.0	1.4	–
RM 7 post *in situ* XRD	71.5	–	–

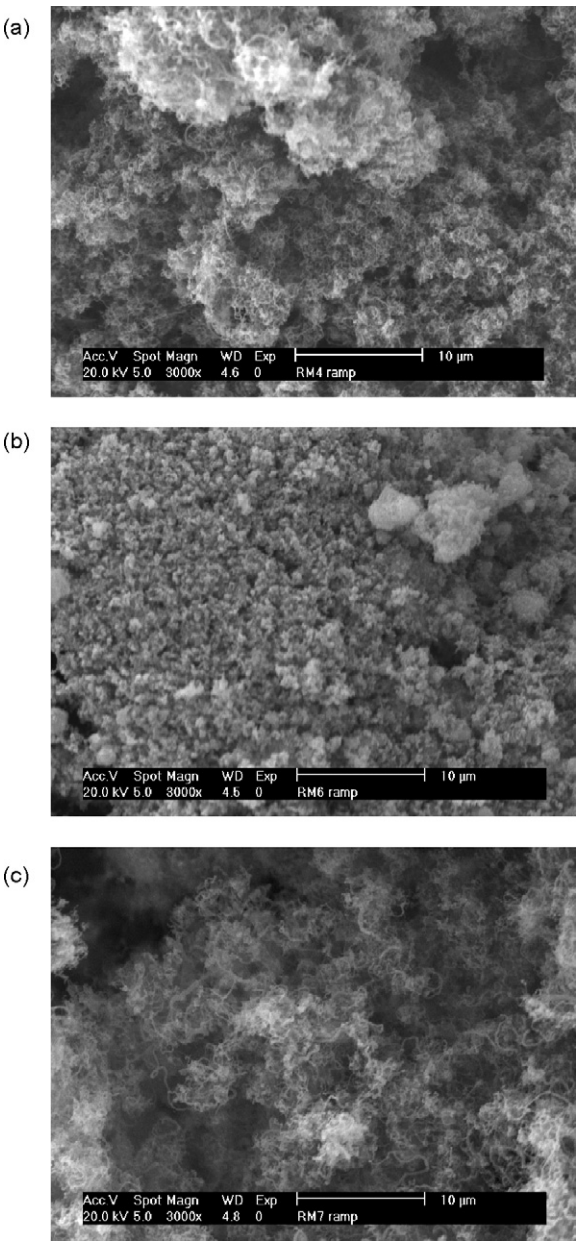

Fig. 3. SEM image after *in situ* XRD in methane for (a) RM 4, (b) RM 6 and (c) RM 7.

3.4. TGA studies

Oxidation of the carbon fibres from the post *in situ* XRD samples in 2% O_2–Ar shows weight loss in the temperature range 500–700 °C (Fig. 4a–c). The profiles of RM 4 and RM 7 are similar. A low level of mass loss occurring over an extended temperature range (ca. 100–450 °C) is initially observed possibly corresponding to the loss of water and/or CO_2, followed by a degree of oxidation of the sample leading to a small increase of mass. A significant loss accounting for most, if not all, of the deposited carbon, is then evident between 500 and 700 °C. The similarity of these profiles is indicative of similar reactivity of the carbon species formed over both materials, although it is apparent that there are differences in the profiles. In the case of RM 4, there is a pronounced asymmetry present in the derivative of the major loss peak which is present to a smaller extent in the RM 7 profile. This may be indicative of different carbonaceous residues of differing reactivity or could arise as the result of the influence of re-oxidation of reduced phases upon the profile.

Table 2
Surface area analysis of red mud samples before and after exposure to *in situ* XRD in methane.

Sample code	BET surface area, m^2/g[a]	
	Pre *in situ* XRD	Post *in situ* XRD
RM 4	12.4	98.1
RM 6	10.1	31.9
RM 7	11.6	70.3

[a] After degassing at 150 °C.

In the case of RM 6, the TGA profile appears very different. While the small degree of mass loss followed by the mass increase occurs (the latter appears larger than in the case of the other two samples, due to the smaller range of its ordinate axis), the mass loss is retarded and is not complete at 800 °C. The reasons for the apparent lower reactivity may be due to the presence of a less reactive form of carbon in this material, the lower surface area of this sample, diffusional limitations or differences in the composition of the precursor red mud. In terms of the latter point, it is important to consider that phases present in the TGA samples may either catalyse or retard oxidation of the carbonaceous species.

3.5. Surface area studies

Table 2 presents the specific surface areas of the sample prior to and after the *in situ* XRD studies. A significant increase in the surface area is observed in case of RM 4 and RM 7, while for RM 6 the increase in the surface area is found to be smaller.

3.6. Formation of carbon oxides

The hydrogen and CO_x formation rates of RM 7 and goethite during methane decomposition at 800 °C were compared in fixed-bed microreactor studies. The mass normalized hydrogen formation rate of RM 7 (Fig. 5a) is similar to that of goethite (Fig. 5b); however, the highest rate was reached in a shorter time in the case of RM 7. The carbon monoxide and carbon dioxide formation rates pass through maxima for both RM 7 and goethite. The production of CO is observed throughout reaction which is indicative of incomplete reduction of the samples and/or of the presence of oxygenates in the feed, although attempts to dry the CH_4 feed via the use of drying tubes were undertaken.

3.7. HRTEM analysis

HRTEM analysis of samples after *in situ* XRD and microreactor studies was undertaken (Fig. 6a–g). While the post *in situ* XRD RM 4 sample showed the presence of CNT, RM 7 mainly consisted of carbon nanospheres. Straight chain bamboo like nanotubes were observed in case of red mud exposed to butane in the fixed-bed microreactor, as discussed later. Fig. 6a shows the TEM images of the carbon formed on RM 4 under a flow of pure methane at 700 °C during *in situ* XRD. The nanotubular carbon observed was primarily parallel walled MWNT (multiwalled nanotubes). The inner-diameter of the hollow nanotubes ranged approximately from 10 to 16 nm, while the outer-diameter ranged from 20 to 40 nm as determined upon a very small fraction of the sample. The length of the nanotubes ran to several micrometers. While in most cases the hollow tubes had open ends, in some cases iron metal could be found in the centre or the end of the tip (Fig. 6b). EDX conducted on the metal particle in the nanotube confirmed the presence of iron. The nanotubes appear as intertwined laces rather than the straight tube like structures which are observed in certain cases. Curvature of the nanotube takes place due to the different catalytic activities on the surface of the nanoparti-

cles causing the tube to bend in the direction of lower growth rate [11].

In case of RM 7, after *in situ* XRD in pure methane, graphite features which grow and encapsulate the particles are seen (Fig. 6c). Nanospheres of various shapes and sizes were observed. In general the diameter of the metal particle enclosed in the carbon nanosphere was larger than that of the particles observed in the case of the nanotubes. The length and breadth of conical nanostructured metal particles was of the order of 100 and 228 nm respectively based on a limited number of observations. A number of graphite layers can be seen encapsulating the central metal particle. In many cases such enclosure of the metal particle has been reported as the main cause of the ultimate deactivation of the catalyst [4]. In certain cases hollow nanospheres were also observed in the samples (Fig. 6d). It has been suggested that the metal particle present in the core of the nanosphere is under pressure and is forced to escape leaving an empty core [6]. The carbon layers then close to form hollow nanospheres.

The morphology of RM 7 exposed to methane in the fixed-bed microreactor experiment was mixed and some angular dense particles were observed which could be iron and/or iron carbide. An interlayer spacing of 3.3 Å between the graphitic layers of the post-reaction RM 7 was measured which corresponds to the ideal graphitic interlayer space (Fig. 6e).

As is common, the goethite precursor has an acicular morphology [20,21], as can be seen by HRTEM (Fig. 6f). Some slit/axial shaped pores running along the axis could be observed, similar to the ones observed by Hirokawa et al. [22]. The formation of the slit like pores is attributed to the evolution of water from the goethite particles [23,24] and this could occur under the influence of the electron beam. The post-reaction sample had very different features compared to the pre-reaction sample (Fig. 6g).

In the post-reaction goethite the acicular morphology was preserved to an extent, although mixed morphologies were observed and the resultant XRD pattern indexes to iron, iron carbide and graphite (Fig. 7).

The formation of MWNT of different morphologies by cracking butane over red mud instead of methane showed the possibility of using different hydrocarbons for obtaining different carbon nanostructures. In the TEM obtained from the post-reaction sample, MWNT with an internal bamboo structure as described by Biddinger et al. [25] were found to be prevalent (Fig. 8a). Similar tubular structures have been observed in studies of methane cracking over Pd/H-ZSM-5 derived catalysts [26]. In addition to graphitic

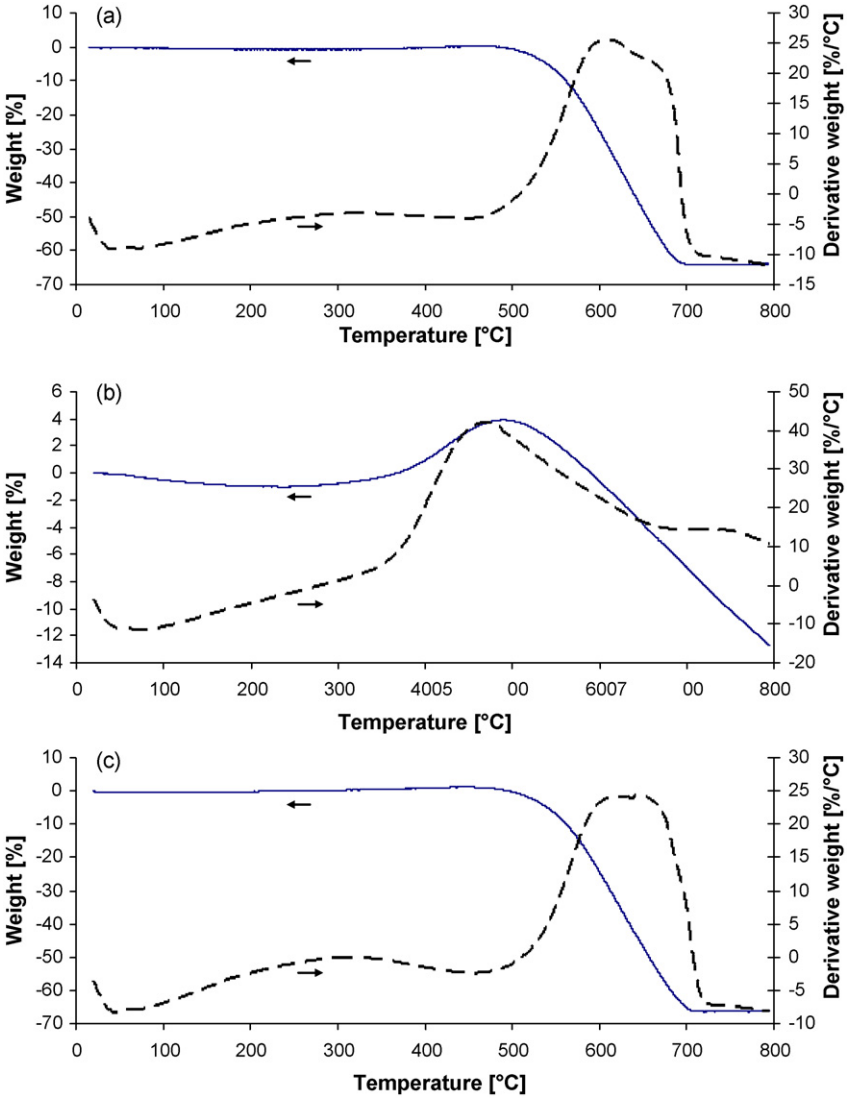

Fig. 4. TGA oxidation profile and corresponding first derivative pattern of (a) RM 4 (b) RM 6 and (c) RM 7, post *in situ* methane decomposition reaction.

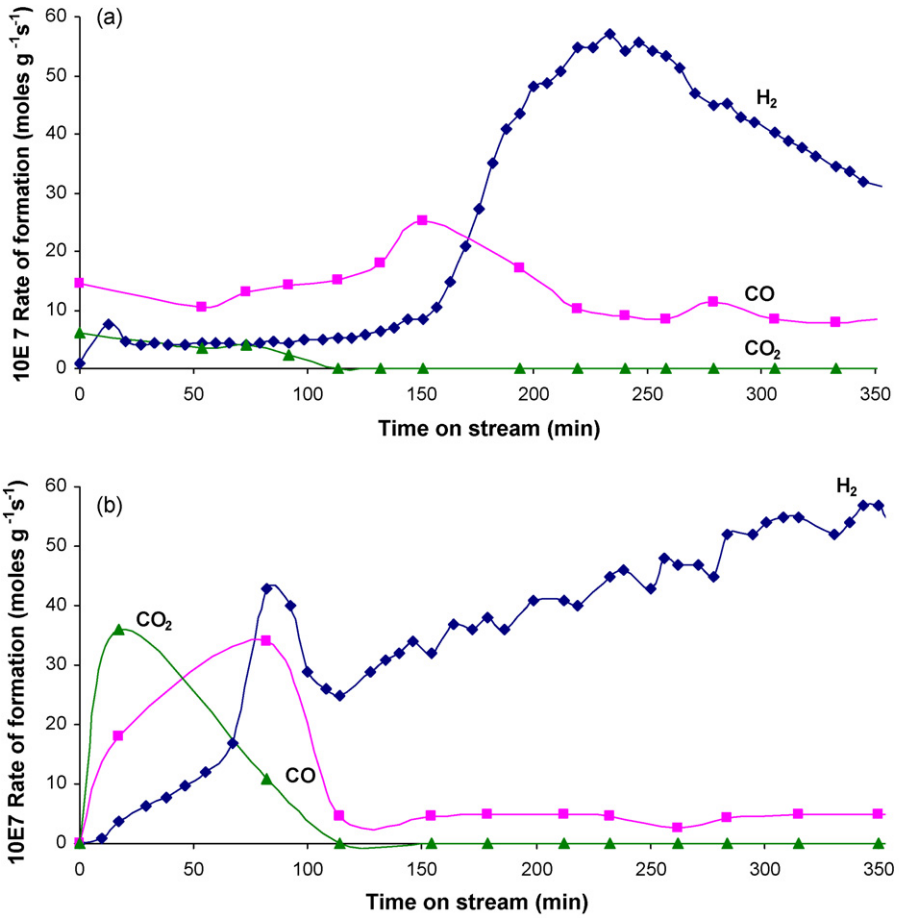

Fig. 5. Mass normalized hydrogen formation rate of (a) RM 7 and (b) goethite at 800 °C.

carbon, traces of amorphous carbon could also be observed on the nanotubes (Fig. 8b). Based upon a limited number of observations, the inner-diameter of the nanotubes ranged between 7 and 22 nm, while the outer-diameter ranged approximately between 110 and 123 nm in size.

4. Discussion

Formation of carbon was observed in all the red mud samples as a result of exposure to methane at high temperatures. However the amount of carbon produced seemed to vary with the composition of the samples. RM 4 and RM 7 showed the maximum growth of carbon, as evident from CHN and SEM analysis, while RM 6 showed very little carbon formation. This led to a lower surface area increase in RM 6 than for the other two samples. For RM 4, the appearance of graphite reflections in the *in situ* XRD reaction runs can be seen at 500 °C; while in RM 6 the peaks are not clear even at 600 °C. RM 4 has the highest Fe_2O_3 content, while RM 6 and RM 7 have lower iron oxide content. As indicated by various studies [27,28] and our own observations, titania is commonly observed to be a constituent of red muds originating in India. The presence of 18.70 wt% TiO_2 in RM 6 may have impeded the reduction of Fe_2O_3 to Fe. In a study by Ermakova et al. [29], Al_2O_3, ZrO_2 and TiO_2 were added as promoting admixtures to determine the effect on the yield and structure of the carbon filaments formed from methane decomposition over iron catalysts. It was observed that the presence of TiO_2 caused an increase in the temperature required for the reduction of the iron oxide. The amount of TiO_2 is very low in RM 7 (0.7 wt%) in comparison to RM 4 which contains 6.44 wt%. This indicates that adverse effects due to the presence of TiO_2 may be very limited in RM 7. However, it is important to note RM 7 contains a significant amount of Na_2O (6.08 wt%), which is known to act as a catalyst poison in methane decomposition [29].

In our study conducted previously, RM 4 was found to be the most active and RM 6 the least active of the samples. Low levels of hydrogen were observed even at 600 °C in the case of RM 4. Upon reaching 700 °C, an increase in the activity was observed. This was in accordance with the iron systems reaching their maximum activity in a "jump like manner" on reaching temperatures higher than 680 °C under methane [29]. Variation in the formation rates of CO, CO_2 and H_2 as a function of time on stream for methane decomposition over iron oxide has been reported in previous studies [30,4]. In the initial stages, the production of CO_2 and CO takes place due to reaction of methane with iron oxide leading to a stepwise reduction of haematite to magnetite, wustite and metallic iron as observed in the *in situ* XRD analysis. Once metallic iron is formed, catalytic decomposition of methane occurs leading to greater hydrogen formation. Alongside the decomposition reaction, the carbon build-up starts and the deactivation of the catalyst begins resulting in reduced hydrogen production.

The carbon nanostructures formed over red mud were observed both by SEM and by HRTEM. Well-structured layers of graphite can be seen forming the tube or sphere like structures. Various types of nanostructures have been reported in the literature [31], and it has been reported that the type of carbon nanostructure formed depends largely on the metal present in the system [32–35,11], the precursor gas used for the reaction [36] and the temperature of reaction. At higher temperatures parallel multiwall structures may be formed while at lower temperatures stacked cone nanotube formation takes place [36].

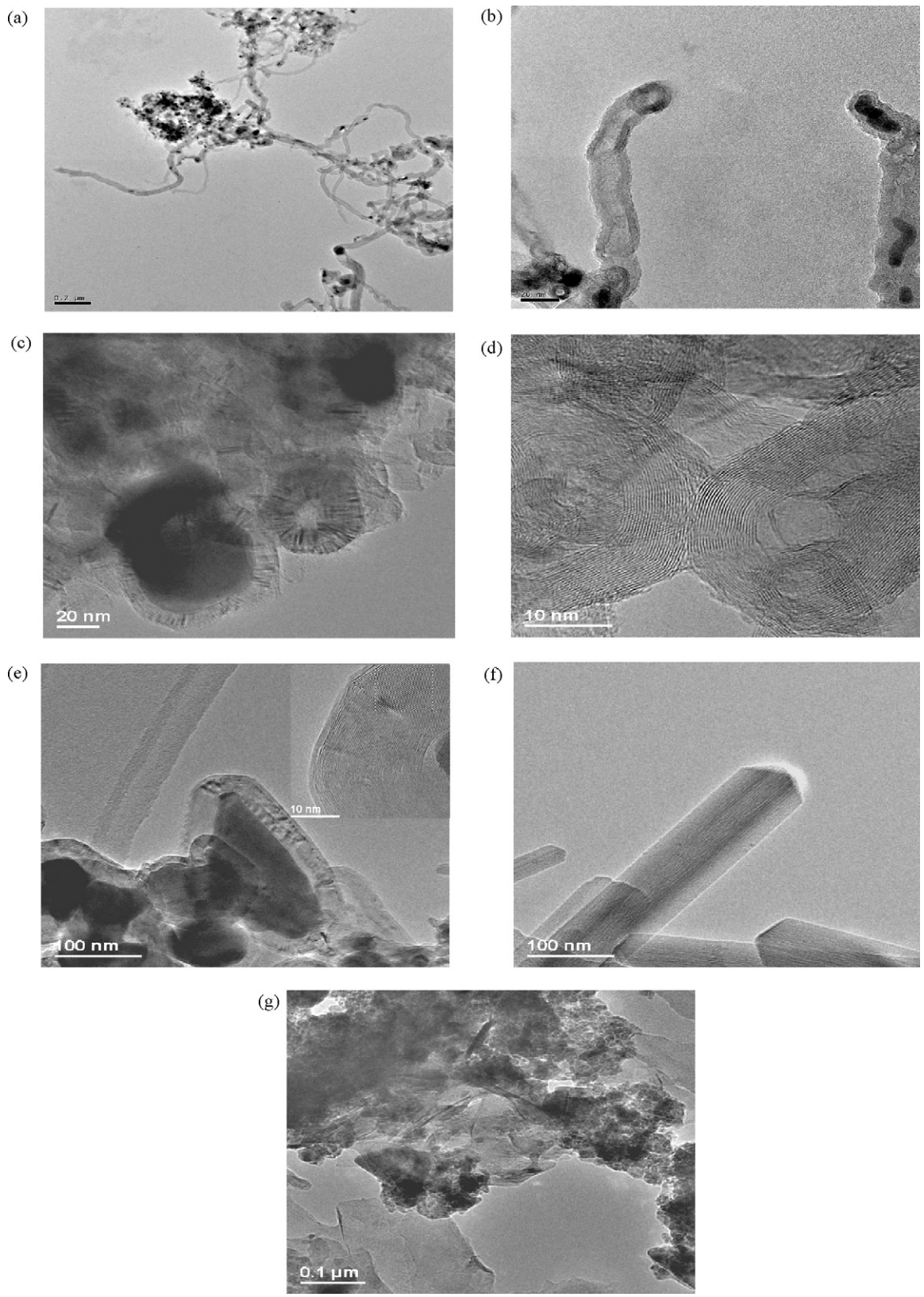

Fig. 6. HRTEM image of (a and b) RM 4 after *in situ* XRD in methane (c) post *in situ* XRD RM 7 showing encapsulated particles with filled/hollow core and (d) hollow cores (e) post-reaction RM 7 (f) goethite precursor and (g) post-reaction goethite.

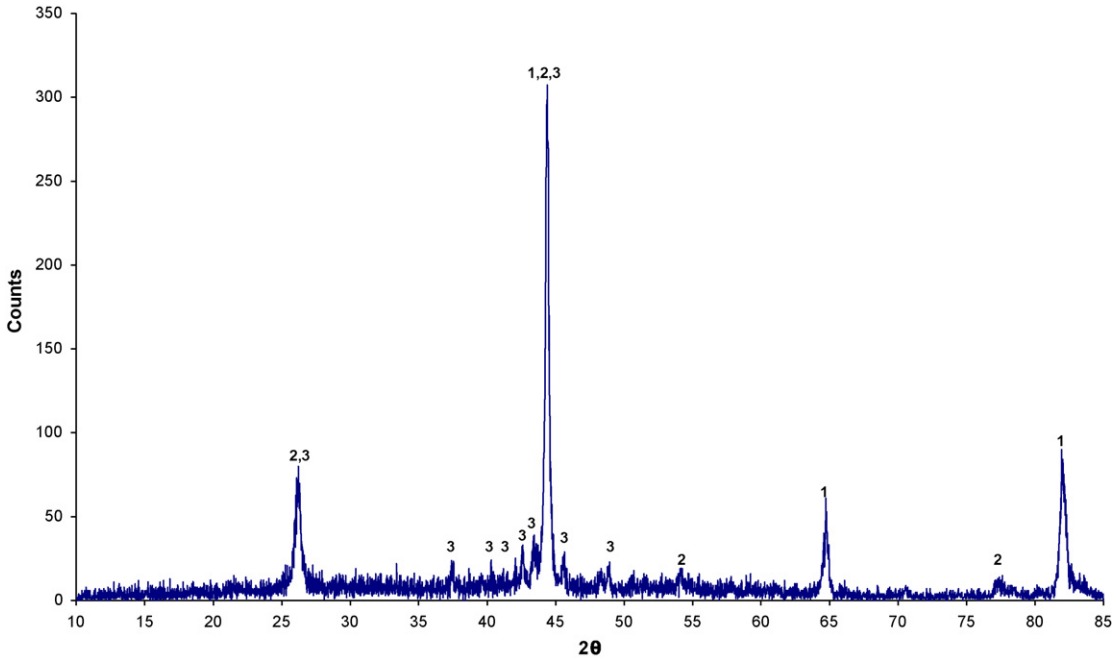

Fig. 7. XRD pattern for post-reaction goethite; 1: iron Fe; 2: cliftonite C; 3: cementite Fe_3C.

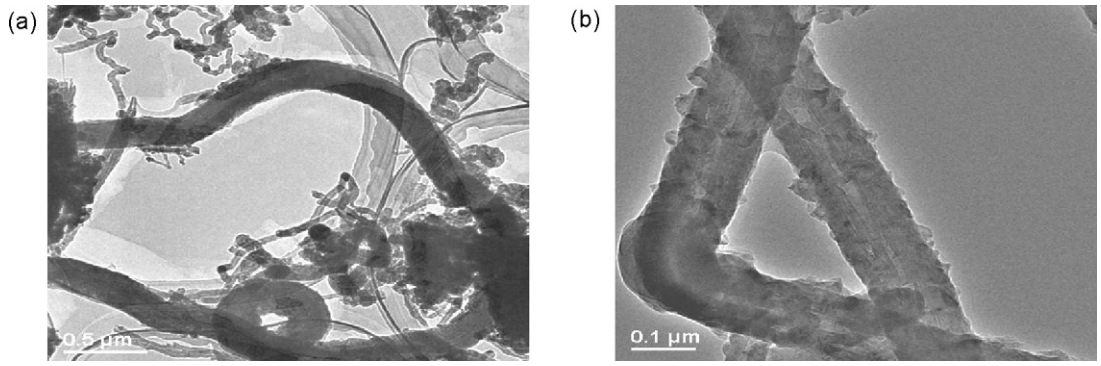

Fig. 8. (a and b) HRTEM of post-reaction red mud sample exposed to butane at 800 °C, showing CNT.

5. Conclusions

In a methane atmosphere, red mud undergoes stepwise reduction at elevated temperature and methane cracking occurs leading to carbon deposition. In the post *in situ* XRD samples graphitic deposits were observed to occur in various forms, as has been reported in methane decomposition studies using transition metal catalysts. Different morphologies were evident including nanospheres and MWNT. Their formation was influenced by the nature of the hydrocarbon source. The red mud samples having significant carbon growth on them have high surface areas and are magnetic. Carbon oxides are formed throughout the reaction, but peak in the initial stages, where significant reduction of the constituent metal oxide phases occurs. Their formation is reduced after the catalytic decomposition of methane starts on the iron formed by reduction of iron oxides and hydroxides.

Acknowledgements

We wish to acknowledge the generous support of the British Council, India for a project grant awarded to MB, VSB, JSJH and IDP under the UKIERI scheme (Project SA07-019). SS gratefully acknowledges the financial support in the form of Senior Research Fellowship provided by CSIR, India. Furthermore, JLR would like to acknowledge the generous support of Conacyt and Universidad Michoacana in allowing him to spend a sabbatical period at the University of Glasgow. Use of the HRTEM Facility Unit, Nanoscience and Nanotechnology Initiative at IIT Delhi (Project No. SR/S5/NM-22/2004) of the Department of Science and Technology, Government of India is also gratefully acknowledged. JSJH also gratefully acknowledges access to the EPSRC TEM Access Facility at the University of St. Andrews.

References

[1] A.F. Cunha, J.M.M. Órfão, J.L. Figueiredo, Catalytic decomposition of methane on Raney-type catalyst, Appl. Catal. A: Gen. 348 (2008) 103–112.
[2] T.V. Choudhary, D.W. Goodman, Methane decomposition: production of hydrogen and carbon filaments, Catalysis 19 (2006) 164–183.
[3] L.B. Adeeva, T.V. Reshetenko, Z.R. Ismagilov, V.A. Likholobov, Iron containing catalysts of methane decomposition: accumulation of filamentous carbon, Appl. Catal. A: Gen. 228 (2002) 53–63.
[4] S. Takenaka, M. Serizawa, K. Otsuka, Formation of filamentous carbons over supported Fe catalysts through methane decomposition, J. Catal. 222 (2004) 520–531.
[5] T. Baird, R. Fryer, B. Grant, Carbon formation on iron and nickel foils by hydrocarbon pyrolysis-reactions at 700 °C, Carbon 12 (1974) 591–602.
[6] J.L. Kang, J.J. Li, X.W. Du, C.S. Shi, N.Q. Zhao, L. Cui, P. Nash, Synthesis and growth mechanism of metal filled carbon nanostructures by CVD using Ni/Y catalyst supported on copper, J. Alloy Compd. 456 (2008) 290–296.

[7] C. Emmenegger, J.M. Bonard, P. Mauron, P. Sudan, A. Lepora, B. Grobety, A. Züttel, L. Schlapbach, Synthesis of carbon nanotubes over Fe catalyst on aluminium and suggested growth mechanism, Carbon 41 (2003) 539–547.
[8] N.M. Rodriguez, A review of catalytically grown nanofibers, J. Mater. Res. 8 (1993) 3233–3250.
[9] L.Z. Gao, L. Kiwi-Minsker, A. Renken, Growth of carbon nanotubes and microfibers over stainless steel mesh by cracking of methane, Surf. Coat. Tech. 202 (2008) 3029–3042.
[10] M.A. Ermakova, D.Yu. Ermakov, Ni/SiO_2 and Fe/SiO_2 catalysts for the production of hydrogen and filamentous carbon via methane decomposition, Catal. Today 77 (2002) 225–235.
[11] N. Zhao, Q. Cui, C. He, C. Shi, J. Li, H. Li, X. Du, Synthesis of carbon nanostructures with different morphologies by CVD of methane, Mater. Sci. Eng. A 460–461 (2007) 255–260.
[12] J. Yang, B. Xiao, Development of unsintered materials from red mud wastes produced in the sintering alumina process, Constr. Build. Mater. 22 (2008) 2299–2307.
[13] S. Wang, H.M. Ang, M.O. Tade, Novel applications of red mud as coagulant, adsorbent and catalyst for environmentally benign processes, Chemosphere 72 (2008) 1621–1635.
[14] Y. Pontikes, C. Rathossi, P. Nikolopulos, G.N. Angelopoulos, D.D. Jayaseelan, W.E. Lee, Effect of firing temperature and atmosphere on sintering of ceramics made from Bayer process bauxite residue, Ceram. Int. 35 (2009) 401–407.
[15] U. Narkiewics, W. Arabczyk, W. Kinicki, Kinetics of carbon deposit formation by methane decomposition on nanocrystalline iron carbide, Fullerenes Nanotubes Carbon Nanostruct. 13 (2005) 99–105.
[16] T.V. Reshetenko, L.B. Avdeeva, Z.R. Ismagilov, V.A. Ushakov, A.L. Chuvilin, Y.T. Pavlyukhin, Promoted iron catalysts of low temperature methane decomposition, Chem. Sust. Dev. 11 (2003) 239–247.
[17] M. Balakrishnan, V.S. Batra, J.S.J. Hargreaves, A. Monaghan, I.D. Pulford, J.L. Rico, S. Sushil, Hydrogen production from methane in the presence of red mud-making mud magnetic, Green Chem. 11 (2009) 42–47.
[18] R.M. Cornell, U. Schwertmann, The Iron Oxides, Structure, Properties, Reactions, Occurrence and Uses, VCH Weinheim, 1996, ISBN: 3-527-28576-8.
[19] A.V. Krestinin, A.V. Raevski, M.B. Kislov, Growth rate of carbon filaments during methane pyrolysis on iron catalyst with analysis using a kinetic-thermodynamic approach, Carbon 46 (2008) 1450–1463.
[20] A.S.C. Brown, J.S.J. Hargreaves, B. Rijniersce, A study of the effect of sulfation on iron oxide catalysts for methane oxidation, Catal. Today 45 (1998) 47–54.
[21] A.S.C. Brown, J.S.J. Hargreaves, B. Rijniersce, A study of the structural and catalytic effects of sulfation on iron oxide catalysts prepared from goethite and ferrihydrite precursors for methane oxidation, Catal. Lett. 53 (1998) 7–13.
[22] S. Hirokawa, T. Naito, T. Yamaguchi, Effect of atmosphere on the goethite decomposition and pore structure of product particles, J. Colloid Interface Sci. 112 (1986) 268–273.
[23] A.S.J. Baker, A.S.C. Brown, M.A. Edwards, J.S.J. Hargreaves, C.J. Kiely, A. Meagher, Q.A. Pankhurst, A structural study of haematite samples prepared from sulfated goethite precursors—the generation of axial mesoporous voids, J. Mater. Chem. 10 (2000) 761–766.
[24] H. Naono, R. Fujiwara, Micropore formation due to thermal decomposition of acicular microcrystals of α-FeOOH, J. Colloid Interface Sci. 73 (1980) 406–415.
[25] E.J. Biddinger, D. Van Deak, U.S. Ozkan, Nitrogen-containing carbon nanostructures as oxygen reduction catalysts, Top. Catal. 52 (2009) 1566–1574.
[26] S. Burns, J.G. Gallagher, J.S.J. Hargreaves, P.J.F. Harris, Direct observation of carbon nanotube formation in Pd/HZSM-5 and MoO_3/HZSM-5 based methane activation catalysts, Catal. Lett. 116 (2007) 122–127.
[27] V.K. Gupta, M. Gupta, S. Sharma, Process development for the removal of lead and chromium from aqueous solutions using red mud—an aluminium industry waste, Water Res. 35 (2001) 1125–1134.
[28] S.S. Amritphale, A. Anshul, N. Chandra, N. Ramakrishnan, A novel process for making radiopaque materials using bauxite-Red mud, J. Eur. Ceram. Soc. 27 (2007) 1945–1951.
[29] M.A. Ermakova, D.Y. Ermakov, A.L. Chuvilin, G.G. Kuvshinov, Decomposition of methane over iron catalysts at the range of moderate temperatures: the influence of structure of the catalytic systems and the reaction conditions on the yield of carbon and morphology of carbon filaments, J. Catal. 201 (2001) 183–197.
[30] M. Gemmi, M. Merlini, U. Cornaro, D. Ghislett, A. Gilberto, *In-situ* simultaneous synchrotron powder diffraction and mass spectrometry study of methane anaerobic combustion on iron-oxide-based oxygen carrier, J. Appl. Crystallogr. 38 (2005) 353–360.
[31] W.Z. Zhou, J.M. Thomas, HRTEM surface profile imaging of solids, Curr. Opin. Solid State Mater. 5 (2001) 75–83.
[32] S.P. Chai, S.H.S. Zein, A.R. Mohamed, A review on carbon nanotubes production via catalytic methane decomposition, in: 1st National Postgraduate Colloquium, School of Chemical Engineering, USM, 2004, pp. 60–69.
[33] X.Z. Liao, A. Serquis, Q.X. Jia, D.E. Peterson, Y.T. Zhu, Effect of catalyst composition on carbon nanotube growth, Appl. Phys. Lett. 82 (2003) 2694–2696.
[34] M.A. Signore, A. Rizzo, R. Rossi, E. Piscopiello, T.D. Luccio, L. Capodieci, T. Dikonimos, R. Giorgi, Role of iron catalyst particles density in the growth of forest-like carbon nanotubes, Diamond Relat. Mater. 17 (2008) 1936–1942.
[35] Q. Li, H. Yan, J. Zhang, Z. Liu, Effect of hydrocarbon precursors on the formation of carbon nanotubes in chemical vapor deposition, Carbon 42 (2004) 829–835.
[36] Y. Wang, W. Shen, N. Shah, F. Huggins, G.P. Huffman, Production of hydrogen and carbon nanotubes by catalytic non-oxidative dehydrogenation of methane and ethane, in: 16th Annual Saudi-Japanese Symposium, Saudi Arabia, November 5–6, 2006.